

# Boundary lubrication with a glassy interface

Anaël Lemaître<sup>(1,2)</sup> and Jean Carlson<sup>(1)</sup>

<sup>(1)</sup> *Department of physics, University of California, Santa Barbara, California 93106, U.S.A. and*

<sup>(2)</sup> *L.M.D.H. - Université Paris VI, UMR 7603,  
4 place Jussieu - case 86, 75005 Paris - France*

(Dated: October 31, 2018)

Recently introduced constitutive equations for the rheology of dense, disordered materials are investigated in the context of stick-slip experiments in boundary lubrication. The model is based on a generalization of the shear transformation zone (STZ) theory, in which plastic deformation is represented by a population of mesoscopic regions which may undergo non affine deformations in response to stress. The generalization we study phenomenologically incorporates the effects of aging and glassy relaxation. Under experimental conditions associated with typical transitions from stick-slip to steady sliding and stop start tests, these effects can be dominant, although the full STZ description is necessary to account for more complex, chaotic transitions.

## I. INTRODUCTION

Advances in developing nanometer scale technologies and devices are intrinsically coupled to fundamental progress in scientific understanding of properties of materials under atomic scale confinement [1, 2, 3, 4, 5, 6, 7, 8, 9, 10, 11, 12, 13, 14, 15, 16, 17, 18, 19, 20, 21, 21, 22, 23, 24, 25, 26, 27, 28, 29, 30, 31, 32, 33]. On one hand, friction, fracture, and plastic deformation at microscopic scales influences the operation and performance of engineered systems. On the other hand, investigation of clean, well characterized nanoscale systems is leading to new insights into these underlying physical phenomena which govern systems under stress.

Increases in scientific computing capacity along with the development of new experimental techniques, has recently created opportunities for progress in both theory and measurements. The surface force apparatus (SFA) was originally designed to study solvation forces induced by a liquid confined between parallel surfaces [1, 2]. Subsequently it was adapted to measure shear forces [3]. The SFA allows precise measurements on a microscopically thin layer of lubricant, separating atomically smooth (typically mica) surfaces. Friction and/or adhesion associated with a single asperity contact can be precisely measured. We focus here on friction and the associated stick-slip instabilities.

In many practical instances friction involves rough materials. However, for rough surfaces it can be difficult to identify underlying mechanisms associated with complex phenomena (e.g. irregular dynamics, and bifurcations). For rough materials individual asperity dynamics are *a priori* combined with any collective phenomena which may be associated with the population of contacts, and the population of contacts itself is necessarily time dependent. Rough surface measurements are thus naturally complementary to investigations of plasticity and rheology of isolated, individual asperities. In addition, for single asperities, effects associated with interfacial materials (e.g. lubricants) are more easily isolated. Furthermore,

there is growing evidence that the frictional properties of rough surfaces even at macroscopic scales is controlled by the plastic deformation of individual contacts. Indeed, experiments have recently been designed which isolate and measure the dynamics of individual asperities at a rough dry interface, subject to shear [34].

In this paper we focus on dynamics of an individual lubricated asperity contact. We model the lubricant using a set of constitutive equations which generalize the shear transformation zone (STZ) theory for amorphous, glassy materials. In addition to the STZ equations, the model incorporates the effects of glassy relaxation *via* the introduction of a state variable related to the internal free-volume (the additional state variable may alternatively be thought of as an out-of-equilibrium effective temperature). The coupled STZ and free-volume dynamics were introduced previously, and shown to capture a range of experimental phenomena in glassy and granular materials [35, 36]. Here the constitutive equations model internal states of the lubricant. We perform a series of analytical and numerical calculations which mimic typical SFA experiments [15, 28, 30], and investigate the stationary states, the bifurcation diagram of the transition between stick-slip and steady sliding, the nature of this transition (i.e. super- or sub-critical), the emergence of chaos, and aging of the yield stress in stop-start tests. At this stage, we primarily map out qualitative behaviors of the model. The compelling correspondence to existing experiments sets the stage for future, more detailed, quantitative comparison with data.

The remainder of this paper is organized as follows. Section II provides a brief overview of friction and boundary lubrication. Section III describes free-volume constitutive equations and summarizes elements of STZ theory. Section IV contains the numerical and analytical results in scenarios representative of SFA experimental studies. Finally, we conclude in Section V with a discussion of our results, comparisons with experiments, and directions for continuing research.

## II. BACKGROUND

In this section we provide a brief overview of boundary lubrication. Our emphasis is on novel material properties and the associated modeling challenges which arise for atomically thin, confined liquid films. Note that, even for interfaces with relatively simple features, we still lack precise quantitative, predictive models for friction. A more complete overview of recent results on friction and lubrication can be found in [12] and references therein.

In boundary lubrication a molecularly thin film of material is confined between two parallel surfaces. The relative motion of the surfaces is mediated by the plastic deformation of the interfacial material lubricating the contact. Molecularly thin films display specific properties which differ from the viscous behavior of bulk materials. Among the most noteworthy of these is the development of a yield stress for thin films at sufficiently low temperatures.

The changes of material properties under confinement can largely be attributed to a liquid-solid transition [5, 8]. In some cases, numerical and experimental evidence suggests layering occurs in the interfacial material [4, 5, 6, 9, 10, 13, 21, 23] and the situation is similar to a liquid-crystal transition. That is, the material orders, and its deformation is expected to result from propagation of dislocations, or layer-over-layer sliding. In other cases, no evidence of ordering of the interfacial material is observed, and the liquid-solid transition induced by confinement enters the very large class of structural glass transitions [10, 11, 22, 32]. In this case the material remains amorphous (liquid-like), but displays solids-like properties. The emergence of a yield stress is accompanied by power-law viscosities, as well as signs of glassy aging [28, 30, 34] and anomalous response spectra [22, 24]. For some lubricants, either a glassy or layering transition can be observed, depending on features such as temperature [32], holding time, surface roughness [37], and commensurability of the surface and the film [23]. Consequences of solid-like ordering within the film include development of a static yield stress, and stick-slip instabilities [14, 15].

Boundary lubrication and the SFA experiments provide special opportunities for theory, because the interface is well characterized and precisely controlled, yet the system is large enough to display phenomena which also arise macroscopically. To date, models have primarily emphasized effects associated with ordering and interactions between the crystalline substrate and the lubricant. These aim to describe effects of layering and surface induced order and involve (i) simple, reduced models of non-interacting particles in an effective periodic potential induced by the surfaces [25], (ii) Ginzburg-Landau functionals which account for heterogeneous ordering [19], or (iii) motion of adsorbate layers in the periodic potential

associated with a regular surface [12, 17, 38].

Alternative approaches focus on internal properties of the lubricant, including contrasts between liquid and solid-like properties and glassy behavior. Phenomenological rate and state friction laws have been introduced [20, 26], in which the friction depends on the instantaneous slip rate and a state variable. The state variable models the collective dependence of friction on the internal degrees of freedom of the lubricant. This approach assumes the fluctuations are sufficiently self-averaging that microscopic degrees of freedom in the boundary layer can be ignored. This simplifying assumption was inspired by a large body of work in dry friction where rate-and-state formulations [39, 40, 41, 42] have shown to be useful to account for experimental data including stick-slip instabilities [43, 44, 45, 46, 47]. State variables can be motivated by experimental observations or molecular dynamics. For dry friction the state variable is related to the average lifetime of individual contacts, whereas in boundary lubrication the state variable is loosely connected to the degree of internal order in the lubricant. However, the friction laws these underlying mechanisms inspire are based more on macroscopic, thermodynamic-like criteria, than on the underlying microscopic physics at the interface.

Our model aims to provide a microscopically motivated description of the macroscopic forces which arise when the amorphous, interfacial lubricant is subject to shear. It relies on the assumption that the deformation of amorphous materials is controlled primarily by excluded volume effects, which dominate over fine details of molecular interactions. This is an old idea, advocated by Struik in the 70's [48], and supported by striking similarities between very different amorphous systems. As a result, a relatively simple account of visco-plasticity is expected to hold for wide classes of amorphous systems. In the conclusion, we discuss how the equations we study here may account for the behavior of not only lubricants, but also sheared granular materials [49, 50, 51, 52].

For the theorist, boundary lubrication has some special, simplifying features which in many respects make it an ideal template to study plasticity of amorphous materials. The interfacial lubricant layer is sufficiently thin that certain bulk phenomena, such as strain localization, appear to be avoided. As a consequence boundary lubrication is, in fact, one of the few experimental setups where *homogeneous* constitutive equations can be directly tested. In contrast, for glassy bulk materials deformation organizes in shear bands, usually a few particle diameters thick, and the strain-rate measured in an experiment averages over a non-uniform field. The origin of strain localization is poorly understood, but clearly a more complete understanding of simple homogeneous flows must be established first. No shear banding is expected to occur in nano-confined films because the deformation is already confined at scales equal to or

smaller than that which would be expected for the shear band. The SFA experimental setup resembles closely the sheared strip used in recent numerical studies of relaxation in glasses [29, 31].

There are, however, several persistent challenges associated with the SFA. Firstly, an astonishingly wide range of phenomena have been observed in this system for different lubricants under different conditions. The range of behaviors remains a puzzle which is difficult to piece together in the absence of a systematic theory that clearly captures the most basic observations. The variability of experimental observations might be attributed to inherent difficulties in the preparation of samples of any glassy material, due to the effects of aging. Certainly capturing the full spectrum of properties is a long term target for theoretical models. Secondly, it is difficult to increase the stiffness of the apparatus beyond  $\sim 3500\text{N/m}$  [53]. A salient feature of boundary lubrication, which directly results from this finite stiffness, is the emergence of stick-slip instabilities at low velocity [5, 7, 14, 15, 28, 30, 32, 54]. In the most dramatic cases, the transition to stick-slip is accompanied by chaotic behavior [30]. The main consequence of the stick-slip instability (and of the finite scanning length of the experimental apparatus), is that the SFA can provide stationary data only for limited ranges of strain-rates. Thus for a wide range of parameters, information about the interfacial material can be gathered only through the observation of instabilities and transient dynamics. Therefore, it is essential to treat this finite stiffness explicitly in any theoretical approach. Ultimately, rather than hampering our understanding of structural glasses, stick-slip instabilities and transient dynamics provide us much richer data than simple stationary states. These instabilities may help clarify important, general issues associated with the out-of-equilibrium properties of structural glasses.

The model we study in this paper is an intermediate statistical theory recently proposed [35, 36, 55] for sheared structural glasses. Here “intermediate” refers to the fact our model falls between the thermodynamic-like, phenomenological rate and state descriptions which have been proposed for friction at dry and lubricated interfaces, and an atomistic statistical mechanical description of the lubricant, which takes into account detailed microscopic, molecular interactions. The model begins with shear transformation zone (STZ) theory [56, 57], which was inspired by molecular dynamics simulations of fracture in amorphous materials, and which provides a microstructural description of shear-induced rearrangements [56, 57, 58]. STZ theory accounts for the emergence of a yield stress in amorphous materials through introduction of state variables characterizing the anisotropy of structural arrangements. Drawing on earlier approaches to describing creep in metallic alloys [59, 60, 61, 62, 63], STZ theory models local shear rearrangements as activated processes, controlled by lo-

cal density fluctuations. This leads to the introduction of free-volume activation factors, in the spirit of early theories of the glass transition [64, 65, 66, 67, 68].

In [35] and subsequent works [36], it was noted that previous approaches treat free-volume as a fixed parameter, although it clearly varies as the material dilates or contracts. In granular materials, for example, density relaxations have been observed and precisely characterized experimentally [69], inspiring several models of slow relaxations [69, 70, 71]. Dilatancy in granular material is also involved in the definition of frictional properties and stick-slip transitions [72]. Slow relaxation of volume or enthalpy are ubiquitous features accompanying the glass transition [48]. We expect more explicit modeling of the time-dependence of density fluctuations may capture the emergence of a wide range of glassy properties near a jamming transition. The constitutive equations introduced in [35] were thus developed to address the question: How much glassy phenomenology can be captured by the simplest account of free-volume dynamics, coupled to the dynamics of shear transformation zones?

Previously it was shown that free-volume dynamics suffices to characterize aging and power law rheologies, while the dynamics of shear transformation zones are required to account for the emergence of a yield stress [36]. In transient regimes, both processes may interact and contribute to rheological properties. Furthermore, chaotic behavior has been observed in the SFA close to the stick-slip instability [30], and it is known in over-damped frictional equations, that two or more state variables are necessary to understand the occurrence of chaos. Here, we did not invoke an *ad hoc* theory with multiple state variables [73], by were led to it by the underlying physical mechanisms already associated with other, relevant experimental observations. Moreover, as chaos is difficult to characterize experimentally, significant insight is provided when observations are supplemented with theoretical models, to guide measurements and analysis.

Finally, we note that it is not *a priori* necessary to identify the additional state variable as a free-volume. It was previously noted by Falk and Langer that free-volume was related to the notion of Edwards’ temperature [56, 74, 75, 76]. As noted later [36], the essential feature that free-volume dynamics captures is the existence of an intensive quantity which measures internal disorder, and which evolves as the system orders or is driven away from equilibrium. Alternative approaches characterize the internal state in terms of an effective temperature [55]. The similarity between free-volume and a temperature results from the fact that, in hard-sphere materials at constant pressure, the dominant contribution to the energy of a subset of molecules is enthalpy. In this case, local energy and density fluctuations are directly correlated. Note finally, that the concept of Edwards’ temperature is likely to be related to effective

temperatures arising in weak versions of the fluctuation-dissipation theorem [77, 78, 79, 80]. In this paper, we use free-volume terminology, and refer the reader to [55] where the relation between free-volume and effective temperature is discussed in more detail.

### III. CONSTITUTIVE EQUATIONS

Our presentation of the model is broken down into four steps: (i) preliminaries associated with the SFA, explicitly accounting for the finite stiffness, (ii) STZ theory, (iii) free volume equations, and (iv) rescaling to obtain dimensionless equations. The equations in sections (ii-iv) have been presented elsewhere, but we include their derivation for the sake of completeness. We refer the reader to [56] and [36, 55] for more detailed discussions of the underlying assumptions.

#### (i) Surface Force Apparatus

A primitive model of the SFA consists of a single slider block, pulled along a surface by a spring of stiffness  $k$ . The opposite end of the spring advances at a prescribed velocity  $V$ . Letting  $x$  denote the displacement of the block relative to the stationary surface, the spring exerts a force  $F = k(Vt - x)$ , where  $t$  is time measured from some initial time  $t = 0$  when  $x = 0$ . The block is subject to both the pulling force from the spring and frictional resistance at the surface. Modeling the SFA as a single slider assumes that the sliding surface is sufficiently small, rigid, and uniform and that friction at the contact is sufficiently self-averaging that slip occurs uniformly across the interface.

Assuming the thickness  $h$  of the interface remains constant, the motion of the slider is related to the rate of shear deformation  $\dot{\gamma}$  of the interfacial material by,  $\dot{x} = 2h\dot{\gamma}$ . If the area  $S$  of the contact is constant, the shear stress exerted by the slider on the interfacial material can be written,  $\sigma = F/S$ . Furthermore, for the experiments we consider, the friction is sufficiently strong that the motion is overdamped, and inertial forces associated with the nonzero mass of the slider can be neglected. This leads to an equation of motion for the stress:

$$\dot{\sigma} = \mu(\dot{\epsilon} - \dot{\gamma}) \quad (1)$$

with,  $\mu = hk/S$ , and  $\dot{\epsilon} = V/(2h)$ . The motion  $\dot{x}(t)$  of the slider follows from the solution to (1), which depends on how the strain-rate  $\dot{\gamma}$  is related to shear stress  $\sigma$  and the internal state variables.

We next define the constitutive equations which couple free-volume and STZ dynamics. Later we restrict our discussion to subsets and (linearized) simplifications of these equations to isolate effects associated with distinct state

variables and/or nonlinearities, and to illustrate phenomena which require a larger number of state variables to be resolved.

#### (ii) Elements of STZ theory

STZ theory is based on the idea that the macroscopic deformation of an amorphous material results from localized rearrangements involving cooperative molecular motion at mesoscopic scales [81, 82, 83]. The loci of such rearrangements are called shear transformation zones, and the internal state of the system is characterized by their number density. In its simplest form, STZ theory involves only two types of zones (labeled “+” and “-”, with number density  $n_+$  and  $n_-$ , respectively) oriented along the principal axes of the shear stress. Zones of each type transform into one another during an elementary shear. The average strain rate  $\dot{\gamma}$  is given by

$$\dot{\gamma} = \mathcal{A}_0 (R_+ n_+ - R_- n_-) \quad . \quad (2)$$

Here  $\dot{\gamma}$  averages over the populations of zones,  $n_{\pm}$ , that reorient with probabilities  $R_{\pm}$ , respectively.

The important insight Falk and Langer contributed to previous STZ theories was to treat the populations densities  $n_{\pm}$  as state variables, and propose equations of motion for the populations. These take the following form [56, 57]:

$$\dot{n}_{\pm} = -R_{\mp} n_{\mp} + R_{\pm} n_{\pm} + \sigma \dot{\gamma} (\mathcal{A}_c - \mathcal{A}_a n_{\pm}) \quad . \quad (3)$$

The first two terms on the right hand side account for exchanges between the populations of STZ's due to mesoscopic rearrangements, while the last term introduces a coupling with the mean flow, through creation of STZ's at rate  $\mathcal{A}_c$ , and annihilation at rate  $\mathcal{A}_a$ . The equations describe how shear deformations induce small displacements of the molecules, hence creating and destroying shear transformation zones. In this framework, the emergence of a yield stress in amorphous solids at low temperature is associated with the mobilization of zones when stress is applied.

#### (iii) Free-volume activation

In the original formulation of STZ theory, the rates were estimated to be nonlinear functions of stress. Derivation of the rates were based on free-volume activation, as developed by Cohen, Turnbull and coworkers to understand the phenomenology of the glass transition [66, 67, 68]. Specifically, the rates  $R_{\pm}$  were estimated to be of the form  $\exp(-v_0(\pm\sigma)/v_f)$ , where  $v_0$  is a stress-dependent activation volume, and  $v_f$  is a material dependent constant. The detailed formulation of transformation rates  $R_{\pm}$  is not essential to capture the

STZ mechanism for jamming. Instead, a first order approximation for the stress dependence of the rates  $R_{\pm}$  is sufficient [56, 57].

However, for hard-sphere systems, the free-volume  $v_f$  is directly related to the density. There is no reason to believe that it should take a fixed value as a function of pressure and temperature. On the contrary, it is a dynamical quantity which evolves as the material dilates or contracts. This observation naturally leads to dynamical equations for the free-volume, written in analogy with equations of motion for the populations  $n_{\pm}$  [35, 36]. While free-volume accounts for the existence of disorder in molecular packing, the difference in STZ densities describe its anisotropy.

Activation factors depends both on free-volume and stress fluctuations. Assuming these effects are uncorrelated, we express the rates as:

$$R_{\pm}(\sigma, v_f) = R_0 \exp\left[-\frac{v_0}{v_f}\right] \exp\left[\pm\frac{\sigma}{\bar{\mu}}\right] . \quad (4)$$

An elementary shear rearrangement takes a “+” oriented zone to a “-” oriented zone, or vice versa, and occurs if sufficient free-volume (large than  $v_0$ ) is available, and if the virtual work of shear forces promotes the transition in the  $\pm \rightarrow \mp$  direction. The variable  $\bar{\mu}$  is here a scale of forces (not to be confused with the elastic modulus  $\mu$ ) which may depend on temperature, and governs stress activation factors. Note that the introduction of backward and forward jumps is an old idea, already present in Eyring’s theory of viscous liquids [84] or in Spaepen’s approach to creep in metallic glasses [59].

The equation of motion for  $v_f$  is given by

$$\dot{v}_f = -R_1 \exp\left[-\frac{v_1}{v_f}\right] + \mathcal{A}_v \sigma \dot{\gamma} . \quad (5)$$

Here free-volume dynamics involve two competing mechanisms: (i) activated elementary compaction which increase the density, and (ii) the transfer of macroscopic work into enthalpy, which dilates the material. The parameter  $\mathcal{A}_v$  specifies how efficiently the work of external forces is used in dilatancy. The parameter  $R_1$  is an update frequency, which should be of the same order as  $R_0$ ; the activation volume  $v_1$  may differ from  $v_0$ , because the two elementary rearrangements (shear and compaction) involve different relative motion of the molecules, hence different reactional pathways. The ratio  $\kappa = v_1/v_0$  is an essential parameter of the theory, and is expected to depend on the shape of the molecules.

The equations described here correspond to the low temperature limit of a more general set of equations for the dynamics of a disorder temperature [55]. We will restrict our current discussion to this free-volume formulation. As we will show, it captures a wide range of phenomena observed experimentally.

#### (iv) Rescaling and change of variables

For the constitutive equations defined above (equations (2) (3) (5)), it is convenient to introduce reduced variables [56, 57],

$$\Delta = \frac{n_- - n_+}{n_{\infty}} , \quad \Lambda = \frac{n_- + n_+}{n_{\infty}} , \quad \text{and} \quad \chi = \frac{v_f}{v_0} \quad (6)$$

along with the rescaled parameters,  $n_{\infty} = 2\mathcal{A}_c/\mathcal{A}_a$ ,  $\epsilon_0 = \mathcal{A}_0 \mathcal{A}_c/\mathcal{A}_a$ ,  $\mu_0 = 1/(\mathcal{A}_0 \mathcal{A}_c)$ ,  $E_0 = 2\epsilon_0 R_0$ , and  $E_1 = R_1/v_0$ . This change of variables leads to the following set of equations:

$$\dot{\gamma} = E_0 \exp\left[-\frac{1}{\chi}\right] \left( \Lambda \sinh\left(\frac{\sigma}{\bar{\mu}}\right) - \Delta \cosh\left(\frac{\sigma}{\bar{\mu}}\right) \right) \quad (7)$$

$$\dot{\Delta} = \frac{\dot{\gamma}}{\epsilon_0} \left( 1 - \frac{\sigma}{\mu_0} \Delta \right) \quad (8)$$

$$\dot{\Lambda} = \frac{\sigma \dot{\gamma}}{\mu_0 \epsilon_0} (1 - \Lambda) \quad (9)$$

$$\dot{\chi} = -E_1 \exp\left[-\frac{\kappa}{\chi}\right] + \alpha \sigma \dot{\gamma} \quad (10)$$

Equations (7), (8), and (9) – free-volume  $\chi$  in (10) being held constant – are almost identical to the original formulation of STZ theory by Falk and Langer [56, 57]. The variable  $\Lambda$  accounts for the total density of STZ’s. The steady state value  $\Lambda = 1$  is a stable fixed point. In STZ theory,  $\Lambda$  differs from 1 only in the initial transient, and its initial value is expected to depend on the type of annealing performed during the creation of a glass from a high temperature liquid. Here we are not concerned with transient features associated with these annealing-dependent initial values of  $\Lambda$ , and will assume  $\Lambda = 1$  throughout. This eliminates equation (9). The variable  $\Delta$ , is a normalized difference “+” and “-” STZ densities. It accounts for the anisotropy of the molecular structure. For a fixed applied stress  $\sigma$  (and fixed free-volume,  $\chi$ ), equations (7) and (8) were shown previously to account for a transition between an elastic regime (jamming) and a visco plastic regime (flowing). The transition occurs at a yield stress,  $\sigma_y$ , satisfying

$$\tanh\left(\frac{\sigma_y}{\bar{\mu}}\right) = \frac{\mu_0}{\sigma_y} . \quad (11)$$

The variable  $\chi$  is a normalized free-volume, which accounts for the existence of disorder in the molecular structure. Its dynamics, determined by equation (10), couples with equations (7) and (8) only as far as  $\chi$  appears in the prefactor of equation (7), setting the time scale of elementary shear events.

At a fixed applied stress  $\sigma$ , equation (7), (8) and (10) account for plastic deformation resulting from the coupled dynamics of  $\Delta$  and  $\chi$ . When the system is driven at a constant shear rate as in the SFA, these equations must

be supplemented with equation (1), which accounts for coupling of material deformation with a compliant driving apparatus.

### Discussion

Most of the results presented here are consequences of free-volume dynamics (10) coupled to equation (7), the STZ variables  $\Delta$  (and  $\Lambda$ ) being held constant ( $\Delta = 0$  and  $\Lambda = 1$ ). In this case, the equations (7) and (10) reduce to:

$$\dot{\gamma} = E_0 \exp \left[ -\frac{1}{\chi} \right] \sinh \left[ \frac{\sigma}{\bar{\mu}} \right] \quad (12)$$

$$\dot{\chi} = -E_1 \exp \left[ -\frac{\kappa}{\chi} \right] + \alpha \sigma \dot{\gamma} \quad (13)$$

These equations can also be linearized for small stresses, which enables us to eliminate the parameter  $\bar{\mu}$  (taken to unity) which enters the exponential activation factors to fix a scale of stresses. The linearized (in  $\sigma$ ) equations are

$$\dot{\gamma} = E_0 \exp \left[ -\frac{1}{\chi} \right] \sigma \quad (14)$$

$$\dot{\chi} = -E_1 \exp \left[ -\frac{\kappa}{\chi} \right] + \alpha \sigma \dot{\gamma} \quad (15)$$

We refer to this as the *stress-linear* approximation. It captures most of the phenomenology accompanying the stick-slip instability, and allows for interesting analytical calculations.

Throughout this paper, we will use these three sets of equations– the full, coupled system of equations including STZ and free-volume effects, the nonlinear equations describing free volume dynamics only, and the linearized version of the free-volume equations– in order to clarify the consequences of our assumptions and the role of the different state variables. The questions raised are: What behavior is already captured by free-volume dynamics, in the stress-linear version (equations (14-15))? What is the importance of activation factors, and the non-linear dependence of strain-rate versus stress (equations (12-13))? What are the expected consequences of the interaction between several internal state variables, as modeled by equations (7), (8) and, (10)?

## IV. COMPARISON WITH EXPERIMENTS

In this section, we compare the qualitative behavior of our model with several important experimental observations. Most of our investigation focuses on the equations governing free-volume dynamics, either in their non-linear form (12-13) or in their linear form (14-15). We study (i) stress versus strain rate relations in steady sliding, (ii) transient dynamics upon start-up, and (iii)

the transitions to stick-slip at low velocities. In the last part of our work, we focus on the existence of (iv) chaotic regimes of stick-slip. In order to observe chaos, we need the full (three-dimensional) set of non-linear equations (7-10).

### (i) Steady sliding

The first step in characterizing the behavior of sheared materials is, of course, the steady state relation between stress and strain rate. In boundary lubrication and single asperity friction, it has been observed that, at low velocities, the friction force is weakly velocity weakening. This weak dependence is reminiscent of the original observations by Dieterich [39, 40] in the case of dry surfaces, where a logarithmic dependence can be assumed with a reasonable degree of confidence. In boundary lubrication and single asperity friction there is insufficient data to conclusively determine whether the steady state relation between force and velocity is logarithmic, power law, or a combination of the two [28, 34]. Below we calculate the stress vs. strain rate relationship in order of increasing model complexity, beginning with the linearized free-volume equations, followed by the nonlinear free volume equations, and finally for the complete model, including STZ's.

#### *Stress-linear equations*

In the stress-linear version of our model (equations (14) and (15)) the ratio between stress and strain rate determines a viscosity,

$$\eta = \exp(1/\chi)/E_0 \quad (16)$$

which is a simple function of the free-volume  $\chi$ .

Initially, we take the limit of infinite stiffness for the experimental apparatus, so that, from equation (1),  $\dot{\gamma} = \dot{\epsilon}$ . From equations (14) and (15), the dynamics of  $\chi$  reduces to:

$$\dot{\chi} = -E_1 \exp \left[ -\frac{\kappa}{\chi} \right] + \frac{\alpha}{E_0} \exp \left[ \frac{1}{\chi} \right] \dot{\epsilon}^2 \quad (17)$$

The quantity  $\chi$  admits a steady state value only if the shear rate is not too large. For high shear rates,

$$\dot{\epsilon} > \dot{\epsilon}^* = \sqrt{\frac{E_0 E_1}{\alpha}} \quad , \quad (18)$$

this equation becomes unstable,  $\dot{\chi}$  is positive at all times, and  $\chi$  diverges. This instability is not related to stick-slip, since it occurs for any value of the stiffness. It indicates that at large shear rates, the material cannot dissipate the work of external forces, and is driven towards a highly disordered state. Situations when  $\dot{\epsilon} > \dot{\epsilon}^*$  are by

definition transient: the material does not reach a steady state. Instead  $\chi$  diverges.

Interpreting  $\chi$  as a free-volume, this divergence may correspond to an opening of the interface, and possible loss of contact between the surfaces. In typical experiments, if such high shear rates are applied, the divergence of  $\chi$  would be *a priori* limited by the scanning length of the experimental device. It is intriguing, however, that opening modes at large shear rates are observed experimentally [53]. They have not been characterized in the literature because they are usually viewed as experimental technicalities which limit the range of accessible driving velocities. Instead, experiments have been restricted to situations in which such effects do not occur, specifically low driving shear rates,  $\dot{\epsilon} < \dot{\epsilon}^*$ , or high shear rates on limited scanning lengths. In the latter case, the apparent viscosity,  $\eta = \exp(1/\chi)/E_0 \sim 1/E_0$  is approximately independent of  $\chi$ , and it may appear, from a measurement of stress alone, that the system is stationary although the internal dynamics may not have reached a steady state.

The existence of this divergence at a critical driving shear rate  $\dot{\epsilon}^*$  arises physically from the fact that the transition probabilities are bounded. The factor  $\exp(1/\chi)$  approaches unity at high  $\chi$ , and becomes increasingly sensitive to changes in the intensive variable  $\chi$  when  $\chi$  is much larger than 1. At this point, free-volume dynamics is only weakly coupled to the other equations. Of course, if a high shear rate  $\dot{\epsilon} > \dot{\epsilon}^*$  is applied steadily, this divergence ultimately leads (in the  $t \rightarrow \infty$  limit) the system towards a highly disordered, “fluidized”, state. Our equations are not designed to describe this limit, and instead should start to break down when  $\chi$  reaches some large values, say  $\chi_f$ . We expect  $\chi_f \gg 1$  (here the value 1 corresponds to the activation free-volume for an elementary shear transformation, which is much less than one molecular volume per molecule, whereas  $\chi_f$  is of the order of one additional molecular volume of free space per molecule). We do not attempt to account for the late stages of this divergence, and only changes of material behavior around  $\chi \sim 1$  are of interest to us. For this reason, and to simplify the discussion, we can safely take  $\chi_f$  to infinity.

We could avoid explicit reference to such a divergence as several mechanisms could be invoked to explain the saturation of free-volume at high velocity resulting in the emergence of another fixed point. Possible mechanisms include: weak density dependencies of various parameters, like  $E_0$ ,  $E_1$ , or  $\alpha$ , or higher order terms in the free-volume dynamics (equation (10), (13), or (15)). Here we study free-volume dynamics in the simplest form for several reasons. Firstly, several mechanisms could be invoked to account for the saturation of free-volume at high velocity, and it is unclear at this stage which would be dominant. Thus we prefer not to differentiate between them. Secondly, regardless of the mechanism, the ap-

proach to any high free-volume fixed point would, in its early stages, closely resemble the divergence we discuss here. Given the limited span of experiments, we expect our model is relevant to observations which are currently available.

For shear rates smaller than  $\dot{\epsilon}^*$ , free-volume admits a steady state value, and this leads to a relation between stress and strain rate, of the form:

$$\sigma = \frac{\dot{\epsilon}^n}{E_0} \left( \frac{\alpha}{E_0 E_1} \right)^{\frac{n-1}{2}}. \quad (19)$$

The constitutive equations thus account for power-law viscosity, with an exponent

$$n = \frac{\kappa - 1}{\kappa + 1} \quad (20)$$

which is directly related to the ratio  $\kappa = v_1/v_0$  of activation volumes. For  $\kappa > 1$  the stress is an increasing function of the shear rate. The material is shear thickening. For  $\kappa < 1$ , the stress is a decreasing function of the shear rate, the material is shear thinning. We will see that, in the later case, the system exhibits a transition to stick-slip at low velocities.

#### Non-linear free-volume equations

Next we calculate the stress vs. strain rate for the non-linear free volume equations (12) and (13). In this case, we obtain a generalization of Eq. (19) which is valid beyond the range of small stresses, where the linear stress approximation is expected to hold. The resulting relationship is given by:

$$\dot{\epsilon} = E_0 \left( \frac{\alpha E_0}{E_1} \right)^{\frac{1}{\kappa-1}} \sigma^{\frac{1}{\kappa-1}} \left( \sinh \left( \frac{\sigma}{\bar{\mu}} \right) \right)^{\frac{\kappa}{\kappa-1}}. \quad (21)$$

For small  $\sigma$  linearization of the hyperbolic sine, leads to the power law rheology described above (Eqs. (19–20)). For large stresses, the right hand side is dominated by the exponential growth in the hyperbolic sine, which results in a logarithmic dependence of the stress  $\sigma$  on strain rate  $\dot{\epsilon}$ . This expression is compatible with experimental observations, although as already mentioned, the range of available observations is sufficiently limited to render detailed functional fits inconclusive [28, 32, 34].

As in the linearized case, Eq. (21) is accompanied by a condition imposed on the strain rate  $\dot{\epsilon}$  which must be satisfied for there to be a self-consistent, steady state value of  $\chi$ . Violation of the condition ( $\dot{\epsilon} > \dot{\epsilon}^*$ ) is associated with diverging free volume and fluidization. For the nonlinear free volume equations the constraint is more complicated than in the linearized case, and is described by  $\dot{\epsilon}/(E_0 \sinh(\sigma/\bar{\mu})) = \exp(-1/\chi) < 1$ . A stationary

value of  $\chi$  exists if and only if the inequality is satisfied. Equivalently, a solution exists iff:

$$\left(\frac{\alpha E_0}{E_1} \sigma \sinh\left(\frac{\sigma}{\bar{\mu}}\right)\right)^{\frac{1}{\kappa-1}} < 1 \quad . \quad (22)$$

The case of equality in Eq. (22) can be used to define a critical value  $\sigma^*$ :

$$\frac{\alpha E_0}{E_1} \sigma^* \sinh\left(\frac{\sigma^*}{\bar{\mu}}\right) = 1 \quad . \quad (23)$$

Then, validity of Eq. (22) depends on the value of  $\sigma$  relative to  $\sigma^*$ . If  $\kappa < 1$ ,  $\sigma$  is a decreasing function of  $\dot{\epsilon}$ , and the condition (22) is met for  $\sigma > \sigma^*$ , or equivalently,  $\dot{\epsilon} < \dot{\epsilon}^* = \dot{\epsilon}(\sigma^*)$ . If  $\kappa > 1$ ,  $\sigma$  is an increasing function of  $\dot{\epsilon}$ , and the condition (22) is met for  $\sigma < \sigma^*$ , or  $\dot{\epsilon} < \dot{\epsilon}^*$ . In both cases, as with the linear equations, there is a limiting driving strain rate,  $\dot{\epsilon}^*$  above which the material fluidizes, and (in our model) the high-velocity fixed point is sent to infinity. For  $\dot{\epsilon} > \dot{\epsilon}^*$ , as the quantity  $\chi$  diverges, the relation between stress and strain rate reduces to

$$\dot{\epsilon} = E_0 \sinh\left(\frac{\sigma}{\bar{\mu}}\right) \quad . \quad (24)$$

Stress appears to be increasing for large values of the strain rate.

#### Full Free Volume and STZ equations

Finally, we explore the steady state stress vs. strain rate relationship using the complete set of equations (7), (8), (9), and (10). In this case, the steady state relation between stress and strain rate reads:

$$\dot{\epsilon} = E_0 \left(\frac{\alpha E_0 \sigma}{E_1}\right)^{\frac{1}{\kappa-1}} \left(\sinh\left(\frac{\sigma}{\bar{\mu}}\right) - \frac{\mu_0}{\sigma} \cosh\left(\frac{\sigma}{\bar{\mu}}\right)\right)^{\frac{\kappa}{\kappa-1}} \quad . \quad (25)$$

The complete equations capture the physical phenomena of jamming (i.e. the absence of flow), which occurs for stresses smaller than a yield stress,  $\sigma_y$ , which satisfies equation (11). Otherwise, the behavior is very similar to our previous results for the nonlinear free volume equations. For non-vanishing shear rates, we can again define  $\sigma^* > \sigma_y$  as the solution of,

$$\frac{\alpha E_0}{E_1} \left(\sigma^* \sinh\left(\frac{\sigma^*}{\bar{\mu}}\right) - \mu_0 \cosh\left(\frac{\sigma^*}{\bar{\mu}}\right)\right) = 1 \quad (26)$$

and  $\dot{\epsilon}^* = \dot{\epsilon}(\sigma^*)$ . Again, for  $\kappa < 1$ , the stress vs. strain rate relation is decreasing, and for  $\kappa > 1$ , it is increasing. Again, the range of strain rates where steady sliding is reached is bounded by  $\dot{\epsilon} < \dot{\epsilon}^*$ . We see from equation (25) that the STZ dynamics do not significantly change the sliding properties as soon as the relevant values of the stress are large compared to  $\sigma_y$ . This situation is particularly relevant for stick-slip instabilities, which occur for  $\kappa < 1$ , in the low velocity, large stress regime.

#### (ii) Transient Dynamics Characterizing the Approach to Steady Sliding

Next we describe transient effects associated with discrete jumps in the applied strain rate. Both the initialization of the system, as well as several common experimental procedures probing transients under controlled conditions, can be described in this general framework. We first consider the initial, waiting time dependent transients associated with starting the system from rest. This is followed by an examination of the experimental protocol, referred to as stop-start, or slide-hold-slide tests, in which the system is prepared in the steady state before the waiting time begins. For this analysis, we will focus on the linear and nonlinear free volume equations. Inclusion of the STZ terms does not quantitatively alter the results.

#### Transient dynamics upon start-up

In the absence of forcing,  $\sigma = 0$ , the linear and nonlinear free volume equations are equivalent. From equation (10) (or (13), or (15)), the free volume  $\chi$  relaxes to 0. The late stages of this relaxation (as the waiting time,  $t_w$ , goes to  $\infty$ ) are logarithmic in time:

$$\chi(t_w) \simeq \frac{\kappa}{\log(E_1 t_w)} \quad . \quad (27)$$

Simultaneously, as the system becomes increasingly compact, the effective ‘‘viscosity’’ (Eq. (16)) increases:

$$\eta(t_w) \equiv \frac{1}{E_0} \exp\left[\frac{1}{\chi}\right] \simeq \frac{1}{E_0} (E_1 t_w)^{1/\kappa} \quad . \quad (28)$$

The immediate consequence of this time dependent relaxation is that the material displays an age dependent initial value of the stress when shear is subsequently applied.

This is illustrated in Figure 1 where we plot  $\chi$  and  $\sigma$  as a function of time, obtained from the integration of equation (1) coupled to (12) and (13). Distinct peaks correspond to samples of different ages at the onset of the applied strain rate. In every case, the system is initialized at  $t = 0$  with a large value ( $\chi(t = 0) = 10$ ) of free-volume. From time  $t = 0$  to  $t = t_w$ , free-volume relaxes in the absence of applied shear. At time  $t = t_w$ , a strain rate  $\dot{\epsilon}$  is suddenly applied, and held constant from that time on. For each curve, the value of  $t_w$  corresponds to the time when stress begins to ramp up.

The initial increase of the stress is due to the fact that  $\chi$  has relaxed to a relatively small value during the waiting time, resulting in a high effecting viscosity, which resists rapid deformation of the material. When the stress gets large, free-volume increases. The system dilates, and the shear deformation rate increases suddenly, resulting in the observed stress drop.

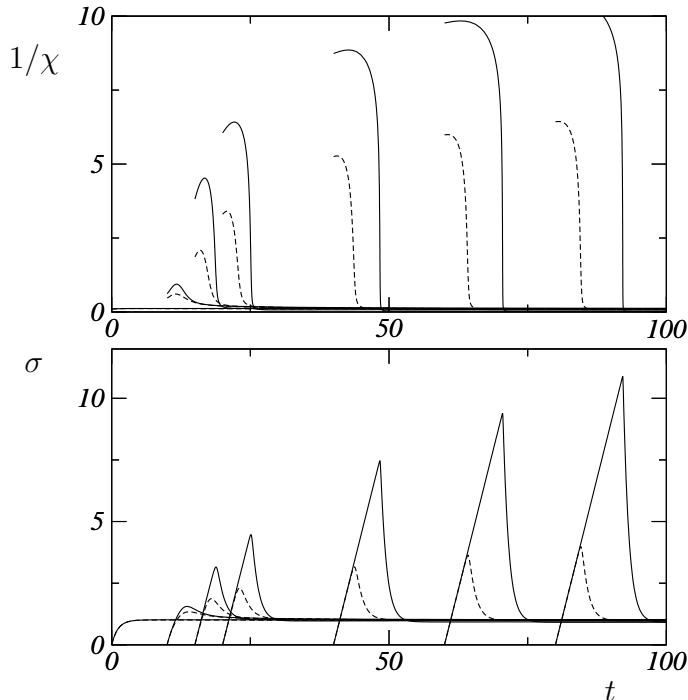


FIG. 1: Transient Dynamics upon start up from the integration of equation (1) coupled to (12) and (13), with  $E_0 = E_1 = \alpha = 1$ . From equation (18),  $\dot{\epsilon}^* = 1$ , and the applied strain rate is  $\dot{\epsilon} = 0.9$ . Results for  $\kappa = 0.8$  (solid lines) and  $\kappa = 1.2$  (dashed lines) are shown. No stress is applied during the initial density relaxation of the material from  $t = 0$  to  $t = t_w$ , marked by the increase of stress. At  $t_w$  the strain rate is suddenly applied and the ensuing dynamics of  $1/\chi$  (top) and  $\sigma$  (bottom) are displayed. Here smaller values of  $\kappa$  (i.e.  $\kappa = 0.8$ ) leads to a larger value of the dynamical yield strength, which results from the fact that a smaller value of  $\chi$  (more compact state) is reached during the waiting period.

#### Stiff apparatus

To provide analytical estimates of the age dependence of the peak stress, we take the limit of an infinitely stiff apparatus,  $\mu \rightarrow \infty$ . When a fixed shear rate is imposed after some waiting time  $t_w$ , the interfacial material resists with a force which is an increasing function of age  $t_w$ . For the linearized equation (14), the stress upon start-up reads,

$$\sigma_{\text{start}}(t_w) = \frac{1}{E_0} (E_1 t_w)^{1/\kappa} \dot{\epsilon} \quad (29)$$

The response is viscous, with an instantaneous initial viscosity which increases as a power of waiting time.

For the nonlinear free-volume equations (12) the power law dependence is replaced by a logarithm. For large  $t_w$ ,

the force upon start-up is:

$$\sigma_{\text{start}}(t_w) \simeq \frac{\bar{\mu}}{\kappa} \log(E_1 t_w) + \bar{\mu} \log\left(\frac{\dot{\epsilon}}{E_0}\right) \quad (30)$$

This logarithmic dependence on waiting time and shear rate at long times is consistent with experimental observations, although it must be noted that experiments performed with the SFA [28, 32] are rather inconclusive and that most significant evidence comes from the single asperity experiments by Bureau *et al* [34]. Here, the logarithmic dependence is a direct consequence of the assumption that transformation rates  $R_{\pm}$  depend exponentially on stress (i.e. proportional to  $\exp(\pm\sigma/\bar{\mu})$ ).

#### Stop-start tests

The characteristics of glassy materials depends sensitively on sample age and preparation methods. It is therefore important to focus on experimental protocols in which the initial state can be relatively well-defined. One common experimental convention which aims to control the initial state involves starting from steady sliding motion. The initial state of the material is determined by the driving velocity. In velocity step experiments the drive velocity undergoes discrete changes from one value to another, and the transient response is monitored. This was one of the original protocols used to investigate the correspondence between rate and state laws and dry friction experiments [39, 40], and was recently investigated for lubricated contacts [28]. Another protocol, referred to as stop-start or slide-hold-slide experiments, involves preparing the system in a constant velocity steady state, then suddenly stopping the drive and letting the system relax for a time  $t_w$ , and finally restarting at the initial velocity. This latter protocol has been studied extensively in boundary lubrication [5, 15, 30], and for the plastic response of single asperities at the contact between rough surfaces [34].

This stop-start protocol grants direct access to the aging process from a well-controlled initial state. Stop-start tests are depicted Figure 2, based on numerical integration of equations (12) and (13) in the limit of an infinitely stiff apparatus. Here  $\chi$  and  $\sigma$  are plotted as functions of time. The initial value of  $\chi$  corresponds to the steady state at a given shear rate  $\dot{\epsilon} = 0.5$ . When the external drive haults (the “stop” phase)  $\chi$  relaxes to a smaller value, as the lubricant becomes more compact. The same shear rate is then suddenly reapplied (the “start” phase) after different waiting times. In this  $\mu \rightarrow \infty$  limit,  $\dot{\gamma} = \dot{\epsilon}$ , and the stress immediately takes its peak value, where the position of the peak marks the waiting time for each curve. After start-up, free-volume increases, due to the transfer of the work of shear forces into enthalpy. This results in a decrease of the viscosity  $\eta$ , accompanied by a decay of the stress with time.

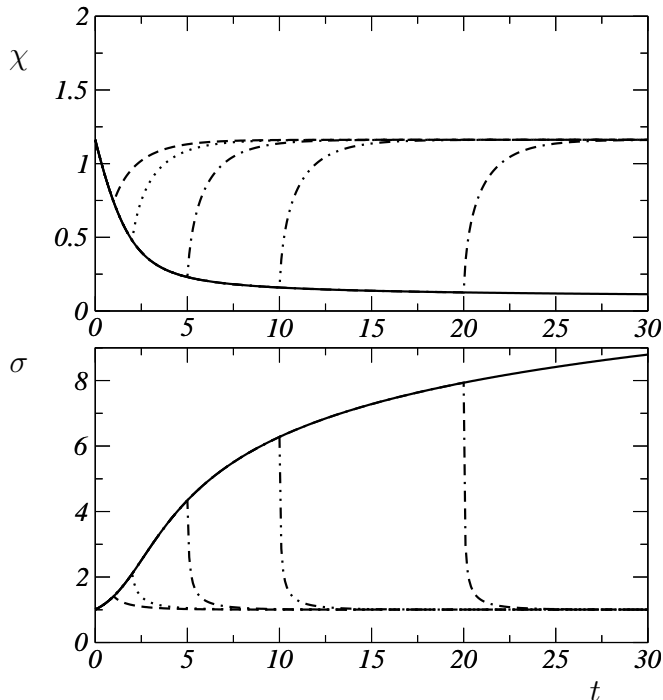


FIG. 2: Numerical integration of equations (12) and (13) during stop-start tests for shear rate  $\dot{\gamma} = \dot{\epsilon} = 0.5$ . Parameters are  $E_0 = E_1 = \alpha = \mu = 1$ , and  $\kappa = 0.8$ . For each curve, the applied shear halts for a time  $t_w$ , after which it is suddenly reapplied. The dynamics of  $\chi$  (top) and  $\sigma$  (bottom) are displayed. The solid lines indicate the relaxation of  $\chi$  in the absence of shear, and the value of  $\sigma$  upon start-up. Different line styles are used for different  $t_w$ .

The solid line in Figure 2 marks the envelope of all response peaks, and thus defines the peak stress as a function of the resting time  $t_w$ . Experimentally, for short waiting times, Yoshizawa *et al.* [15] observed that for certain lubricants, the corresponding curve exhibits a well defined latency time. That is, there is a threshold in the waiting time, below which no increase in the stress is observed. For longer waiting times, Drummond *et al.* and Gourdon *et al.* [28, 32] found that the difference  $\Delta\sigma$  between the peak value of the stress, and the steady state value (the so-called “stiction spike”) increases as  $\Delta\sigma \sim \log(t_w)$  for large  $t_w$ . Both the short and long time behavior is reproduced by the nonlinear free volume equations, as shown in Figure 3 for different values of the driving velocity. Note the latency time (roughly associated with the rapid rise of  $\Delta\sigma$ ) becomes increasingly sharply defined at high drive velocities. This follows from the fact that at high velocities, approaching the limiting shear rate  $\dot{\epsilon}^*$ , the stationary value of free-volume is large, hence free-volume activation factors (which scale as  $\exp(1/\chi)$ ) are essentially constant. Therefore, the free volume the free volume  $\chi$  nearly decouples from the rela-

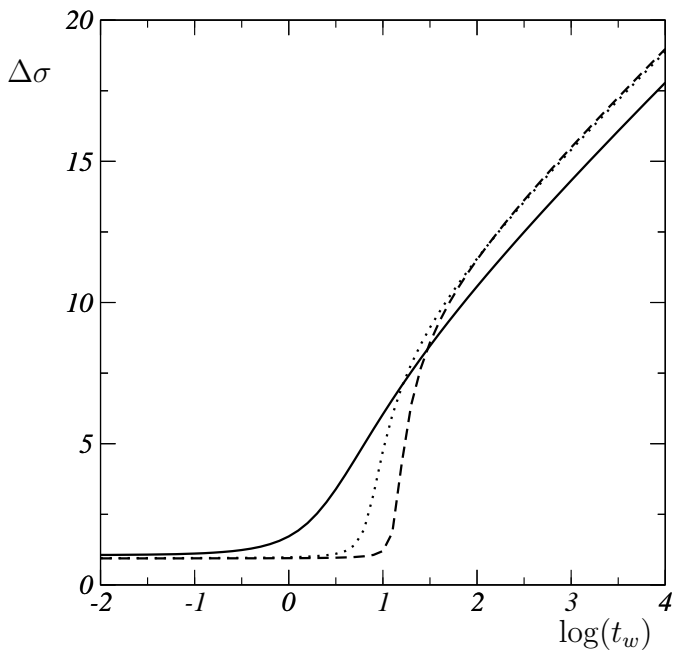


FIG. 3: Peak stress,  $\Delta\sigma$  as a function of waiting time  $t_w$ , from integration of equations (12) and (13). Parameters are  $E_0 = E_1 = \alpha = \mu = 1$ , and  $\kappa = 0.8$ , whence  $\dot{\epsilon}^* = 1$ . Different shear rates have been used:  $\dot{\gamma} = \dot{\epsilon} = 0.3$  (solid line), 0.9 (dotted line) and 0.99 (dashed line). Approaching  $\dot{\epsilon}^* = 1$ , a latency time interval becomes increasingly well defined, indicating the increasing importance of free-volume dynamics beyond the small- $\chi$  domain, where log-time relaxation of free-volume holds.

tion between stress and strain rate. If the external drive is stopped during a short time interval,  $\chi$  relaxes, but the changes in  $\chi$  have little effect on the dynamic viscosity  $\eta$ . Therefore, when the shear is applied again, the relation between stress and strain rate is still very close to steady state, and only a very faint peak is observed.

Note finally that, due to the small spatial extent over which shear can take place in the SFA, it is likely that in some experiments the internal state of the material never reaches the steady state value. It might appear that a steady state has been reached when  $\chi$  is large enough to almost decouple from the stress *vs.* strain-rate relation. In this case, the latency time depends on the time it takes for  $\chi$  to relax to values of order unity, which will depend on the details of sample preparation. This subtle history dependence may explain large fluctuations observed in some experiments [15, 28, 30].

### (iii) Instability and transition to stick-slip

Here, we show that our constitutive equations not only account for the existence of stick-slip behavior at low drive velocity, but that they reproduce the shape of the stick-slip cycle with remarkable accuracy. They also account for the existence of continuous and discontinuous transitions to stick-slip depending on the stiffness of the apparatus, and in some cases, chaos in the neighborhood of the transition. For this analysis, the nonlinear free volume equations will be sufficient to characterize the transition from stick-slip to steady sliding, and the nature of the bifurcation. The full set of coupled constitutive equations, including STZ, preserve the phase boundaries described by the free volume equations. However, STZ effects (particularly, which introduce another dimension to the dynamical system) are required to capture chaotic phenomena.

#### *Stick-slip motion: shape of the pulse*

At low drive velocities, and for a sufficiently compliant apparatus, rather than sliding at constant velocity, the interface exhibits stick-slip motion. We begin our analysis of this motion by illustrating a typical stick-slip cycle obtained from numerical integration of equation (1) coupled with the constitutive equations (12) and (13). In Figure 4 we plot the time series of  $\chi$  and  $\sigma$  during stick-slip. As in the experiments, stick-slip cycles appear qualitatively similar to stiction peaks. However, stick-slip arises when the driving motion is constant, unlike stiction peaks in stop-start test, which represent transient responses to time varying slide-hold-slide drivers and are typically monitored in regime where the steady state motion corresponds to constant velocity sliding. Stick-slip arises due to an internal instability of the material at a given shear rate. Rather than sliding at that steady rate, the material alternates between “sticking” and “slipping.” During the stick phase free-volume decreases to a value which is small enough to hinder the relative displacement of lubricated surfaces, during which time the material creeps at a rate which is too slow to keep up with the external drive. Consequently, the stress builds up. When it becomes large enough to trigger dilatancy, the slip phase begins, and  $\chi$  increases suddenly, and the stress is released during rapid sliding motion.

In Figure 5 the same data is represented in a plot of  $\sigma$  versus  $\dot{\gamma}$ , which compares quite favorably with typical cycles observed by Drummond and Israelachvili [28].

#### *Characterization of the Hopf Bifurcation*

With decreasing velocity and for a compliant apparatus, our constitutive equations exhibit a Hopf bifurcation

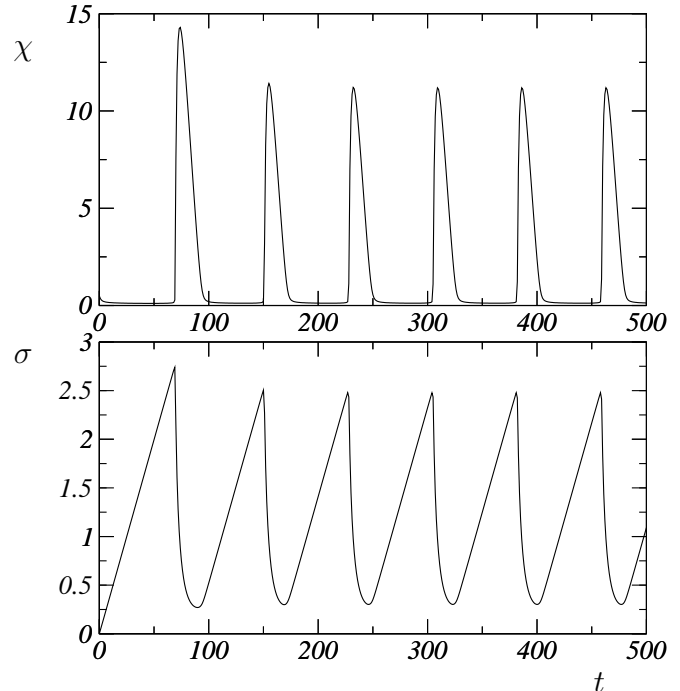


FIG. 4: Stick-slip dynamics obtained from numerical integration of equations (1), (12) and (13) for a fixed strain rate  $\dot{\epsilon} = 0.2$ , and stiffness  $\mu = 0.2$ . Parameters are  $E_0 = E_1 = \bar{\mu} = \alpha = 1$ , and  $\kappa = 0.8$ . The initial value of the free-volume is  $\chi = 1$ . The regime of steady plastic deformation is unstable and leads to stick-slip motion. Fast relaxations of the stress result from sudden dilatancy of the material.

separating steady sliding from stick-slip dynamics. The locus of bifurcation points defines a phase boundary in the  $\mu$  (stiffness) vs.  $\dot{\epsilon}$  (strain rate) plane. A systematic analysis of the emergence of stick-slip motion is easily performed for the stress-linear version of the constitutive equations. The details are given in Appendix I. The critical stiffness defining the Hopf bifurcation point for Eqs. (1), (12) and (13) is given by

$$\mu_{\text{hopf}} = \frac{E_1}{E_0} \frac{1 - \kappa}{(\kappa + 1)^2} \left( \frac{\alpha \dot{\epsilon}^2}{E_0 E_1} \right)^{\frac{\kappa - 1}{\kappa + 1}} \ln \left[ \frac{\alpha \dot{\epsilon}^2}{E_0 E_1} \right]^2. \quad (31)$$

Solving for  $\mu$  as a function of  $\dot{\epsilon}$  with all other parameters held fixed, defines the phase boundary in the  $(\mu, \dot{\epsilon})$  plane, below which steady sliding becomes unstable (see Figure (6)). Our curve exhibits the same convexity as available experimental data [30, 45]. Additional experiments are needed to provide a quantitative experimental characterization of the curve.

Experimental data also suggest that different types of transitions between stick-slip and steady sliding are possible. The transition may be continuous (approaching the phase boundary the amplitude of stick slip motion de-

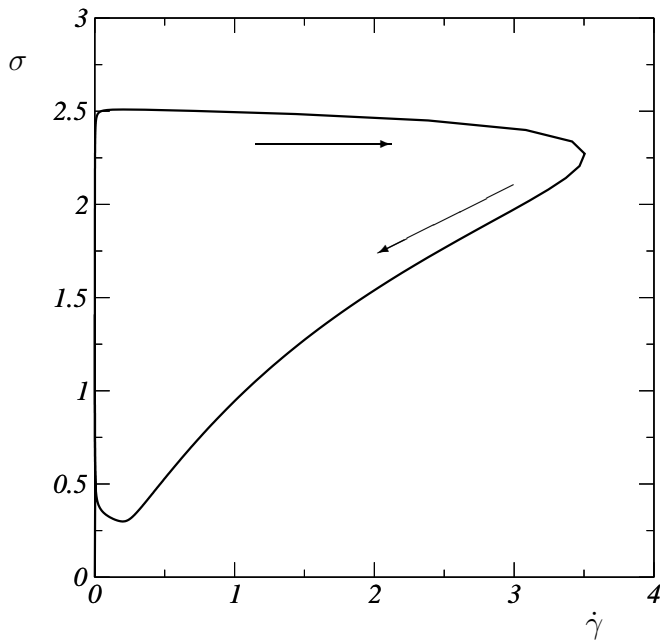


FIG. 5: Stick-slip cycle from the data of Figure 4. Arrows indicate the direction in which the stick-slip cycle is followed. The ramps on Figure 4 correspond here to the increase of  $\sigma$  at vanishing  $\dot{\gamma}$ . The plastic strain rate suddenly increases at almost constant  $\sigma$  before the friction force starts to decrease.

creases continuously to zero as drive velocity is increased) or discontinuous (there is an abrupt change from finite amplitude stick-slip spikes to steady sliding as drive velocity is increased). Continuous transitions correspond to supercritical Hopf bifurcations, and discontinuous transitions correspond to subcritical bifurcations. The latter case is typically accompanied by hysteresis (i.e. coexistence of stick-slip and steady sliding, such that a steady decrease in the drive velocity results in a transition to stick slip at a lower strain rate than that associated with the transition to steady sliding associated with increasing velocity from the stick-slip phase). This feature is observed in both lubricated friction [30] as well as dry interfaces. In the latter case it is better characterized [45], though the physical origin of the similarity (if indeed it persists upon more detailed experimental investigations) remains unclear. For both cases, to date analytical models have failed to capture the existence of both super- and sub-critical Hopf bifurcations.

The transition point separating super- and subcritical Hopf bifurcations on the phase boundary in the  $(\mu, \dot{\epsilon})$  plane depends on third order terms in a normal expansion of the dynamical system around the steady state. Therefore, this property offers a particularly stringent

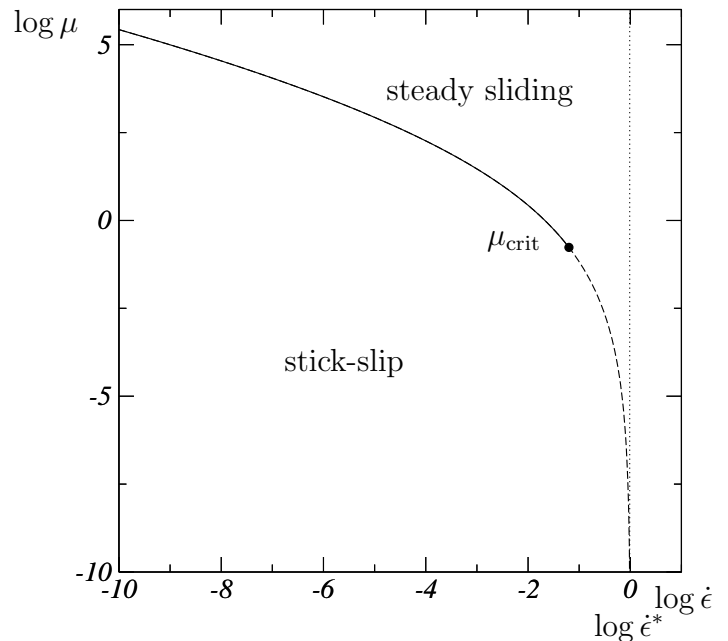


FIG. 6: Phase diagram for equations (1), (14) and (15), and  $\kappa < 1$ , in  $\log \dot{\epsilon}$ - $\log \mu$  plane. The dotted line indicates the limit velocity  $\dot{\epsilon}^*$  beyond which  $\chi$  diverges. The solid and dashed lines denote the curve  $\mu_{\text{hopf}}$  below which steady sliding motion is unstable;  $\mu_{\text{hopf}}$  vanishes at  $\dot{\epsilon} = \dot{\epsilon}^*$ . The solid part of this line corresponds to points where the transition to stick-slip is continuous (super-critical) while the dashed line corresponds to points where the transition is discontinuous (sub-critical). When the transition is discontinuous, there is a zone of bistability, which lies above the dashed line.

test of constitutive equations. We have performed the analysis of the system (1), (12) and (13). Our analysis defines a point:

$$\mu_{\text{crit}} = \frac{E_1}{E_0} \frac{e^{-\kappa + \sqrt{2 - 2\kappa + \kappa^2}}}{1 - \kappa} \left( \kappa - \sqrt{2 - 2\kappa + \kappa^2} \right)^2 \quad (32)$$

on the Hopf line, which is drawn on Figure 6. Above, and on the left of this point, the Hopf bifurcation is supercritical (continuous); below, and on the right of it, the bifurcation is sub-critical (discontinuous).

The shape of the phase boundary as well as the types of transitions, and even their relative placement in the phase diagram are consistent with current experimental observations. However, a complete and quantitative characterization of the phase diagram for boundary lubrication remains an open challenge experimentally. Overcoming obstacles associated with the limited range of stiffness which can be probed with existing techniques will enable key observations which can be compared with both the contrasting case of dry friction experiments and

the theoretical results presented here.

### Chaotic stick-slip

Drummond and Israelachvili [28] observed that in some cases stick-slip motion became erratic in the neighborhood of the transition. These authors identified the erratic motion as *chaotic*, based on the analysis of experimental time series. Their results were indeed suggestive of positive Lyapunov exponents. However, methods to identify chaos based on analysis of an individual experimental time series are necessarily approximate and inconclusive, and alone are insufficient to guarantee that the erratic motion is chaos as opposed to some form of noise amplification.

Given these uncertainties, models can play a special role in helping to differentiate between mechanisms which may lead to chaos vs. other modes of irregular motion. Here we study the full set of nonlinear constitutive equations (1), (7-10), which include the STZ state variables. The dimension of this dynamical system is three, which is the minimum requirement for chaos. As shown below, over a restricted range of parameters, the model admits chaotic solutions, characterized by irregular stick-slip and positive Lyapunov exponents. Because these equations are deterministic, noise amplification is ruled out as a source of irregular motion in the model.

In order to measure Lyapunov exponents we directly integrate the equations of motion of a Lyapunov vector  $u(t)$  in the tangent space (see *e.g.* [85]). The largest Lyapunov exponent  $\lambda$  is estimated from the long-time behavior of the norm of this vector:

$$\lambda = \lim_{t \rightarrow \infty} \frac{1}{t} \log \|u(t)\| \quad . \quad (33)$$

For this numerical study, we used a fourth order Runge-Kutta algorithm with fixed and variable time steps. We checked that the results do not change qualitatively as a function of the precision of our numerical method, as long as the precision is sufficiently high.

Figure 7 shows typical traces in the chaotic regime. The three variables  $\sigma$ ,  $\Delta$ ,  $\chi$ , as well as the value of

$$\lambda(t) \equiv \frac{1}{t} \log \|u(t)\| \quad , \quad (34)$$

are shown. This data illustrates that chaotic stick-slip can arise in this system. Chaos results from the interplay between the dynamics of the variable  $\Delta$ , which characterizes the anisotropy of the molecular packing, and the variable  $\chi$  which characterizes the dilatancy of this packing.

Further investigation reveals that the range of parameters where chaos (i.e. at least one positive Lyapunov exponent) is observed is restricted to a relatively compact area of the  $\mu$  vs.  $\dot{\epsilon}$  phase diagram, which is close

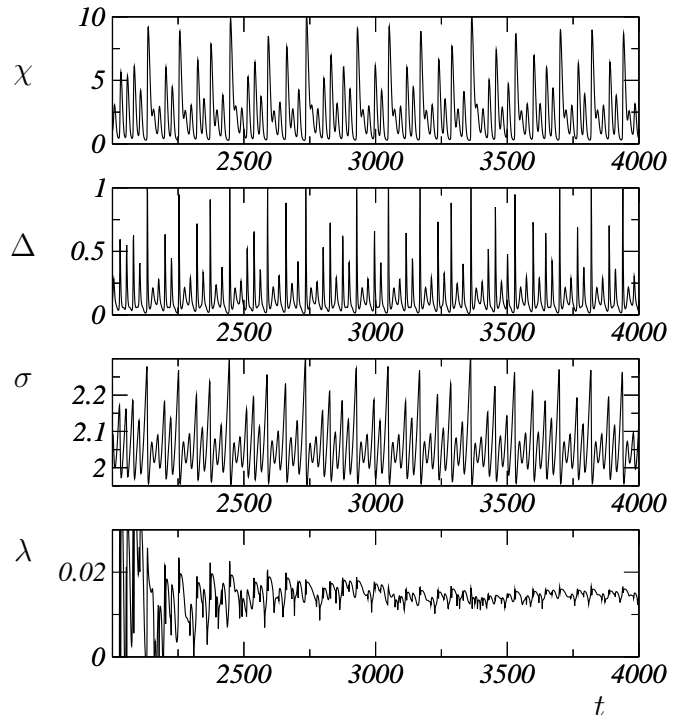


FIG. 7: Chaotic motion:  $\Delta$ ,  $\chi$ ,  $\sigma$  and  $\lambda$  are plotted as a function of time  $t$  for equations (1), (7), (8), (10). for parameters,  $E_0 = 0.5$ ,  $E_1 = 1$ ,  $\epsilon_0 = 1$ ,  $\alpha = 2$ ,  $\mu_0 = 0.5$ ,  $\bar{\mu} = 0.5$ ,  $\mu = 0.14$ ,  $\kappa = 0.8$  and  $\dot{\epsilon} = 0.14$ . The asymptotic limit reached by  $\lambda(t)$  is the largest Lyapunov exponent, which is clearly positive, indicating chaos.

to, but not overlapping the transition from stick-slip to steady sliding, in a region near the critical point separating sub- and super-critical Hopf bifurcations. This relatively restricted range is not surprising. Since chaos requires the dynamical system to be three-dimensional, it may disappear as soon as one variable is enslaved to another. In our case, this decoupling may occur either when the time scale of the dynamics of  $\Delta$  and  $\chi$  are well separated from each other or when the absolute value of  $\Delta$  becomes negligible in equation (7).

To illustrate the chaotic domain, in Figure 8 we present a two-dimensional image illustrating the value of the maximum Lyapunov exponent as a function of the parameters  $\mu$  and  $\dot{\epsilon}$ . In the color map, negative values of the Lyapunov exponent appear in blue, and describe the case of a stable fixed point in the dynamics. This corresponds to steady sliding motion at constant  $\chi$ . This is the solution between the Hopf bifurcation and the  $\dot{\epsilon} = \dot{\epsilon}^*$  line (recall for  $\dot{\epsilon} > \dot{\epsilon}^*$ ,  $\chi$  diverges, and our theory breaks down). In the color map, green corresponds to a zero value of the Lyapunov exponent. The value  $\lambda = 0$  characterizes a time translation invariant manifold. Green thus describes stick-slip regimes, which exhibit a peri-

## V. CONCLUSION

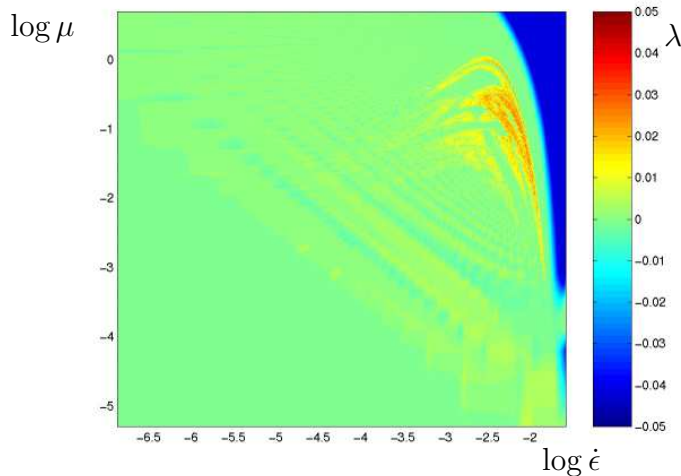


FIG. 8: Two-dimensional plot of the asymptotic Lyapunov exponent in the  $(\log(\dot{\epsilon}), \log(\mu))$ -plane obtained from numerical integration of equations (1, 7-10). The color scale on the right gives the maximum value of the Lyapunov exponent  $\lambda$ , as defined in equation (40). Negative values of the Lyapunov exponent appear in blue: they correspond to steady sliding. The vertical asymptote of the phase boundary as  $\log(\mu) \rightarrow -\infty$  (i.e. roughly the right edge of the figure) corresponds to  $\epsilon^*$ . Periodic stick slip corresponds to green, corresponding to vanishing of the Lyapunov exponent. Chaotic behavior is associated with positive values of the Lyapunov exponent, which appear here in red and yellow. Chaotic regions of stick-slip are separated by windows of periodic motion.

odic limit cycle. Green also appears as the maximum Lyapunov exponent for large values of the driving shear rate ( $\dot{\epsilon} > \dot{\epsilon}^*$ ). In this case, the asymptotic state of the system is not strictly speaking a fixed point, because  $\chi$  is evolving at all times.

Chaotic motion is associated with positive Lyapunov exponents which appear as red or yellow in Figure 8. They occur within the stick-slip portion of the phase diagram, near the transition between super- and sub-critical bifurcations. As shown in the figure, in the model this behavior is clearly separated from the Hopf boundary by a narrow range of regular stick-slip. The close proximity of the chaotic zone to the Hopf bifurcation may explain the fact that experimentally it appears that when chaotic stick-slip is observed, it merges continuously into the Hopf transition. While our equations predict a regular Hopf bifurcation to periodic stick-slip, with chaotic stick-slip resulting from secondary instabilities, the intermediate periodic regime occurs over a sufficiently narrow range that it may be difficult to differentiate experimentally between this case and a case in which the Hopf transition takes place directly via chaotic stick-slip.

We have shown that a limited set of constitutive equations capture at least qualitatively a wide variety of phenomena observed experimentally in single asperity, boundary lubricated friction. Most of the phenomena are captured by the dynamics of a single state variable identified here as free-volume. In steady sliding, the free-volume dynamics account for the existence of velocity-weakening or velocity-strengthening friction laws, involving mixed power-laws and logarithmic dependences. In stop-start experiments, logarithmic increases in the peak stress with increasing hold time results from the relaxation of free-volume, whereas for short hold times a latency time emerges from the non-linearity of the transition rates. The dynamics of free-volume also accounts for the existence of a transition from steady sliding to stick-slip as drive velocity is decreased, and for the presence of both continuous and discontinuous transitions, depending on the stiffness of the driving apparatus. Finally, the complete set of equations where free-volume couples to the dynamics of STZs, accounts for the emergence of chaotic behavior close to the stick-slip transition.

Our present work is in sufficiently close qualitative agreement with experiments to warrant a further round of more quantitative experimental vs. theoretical comparisons. Our work leads to clear predictions for the friction in steady sliding regimes, and the transition to stick-slip as a function of the compliance. Available experimental data provides steady sliding friction over a limited range of velocities, and a collection of stick-slip cycles at low velocities for a given interfacial material, most often for a unique value of the compliance. Available measurements of power-law, or logarithmic relationships between force and driving velocity are not sufficient to validate or invalidate a set of constitutive equations. In principle, we could attempt to directly fit cyclic stick-slip data, but in practice, this is extremely difficult, requiring additional assumptions about initial values of one or more internal variables. What information can we thus use to compare theory and experiments? Compliance is included in the model at a low cost in terms of the assumptions required, yet provides a large panel of predictions which magnify the sensitivities of the constitutive equations and the microscopic assumptions of the theory. The location of the transition to stick-slip, its dependence on compliance, and the type of transitions to stick-slip are important predictions of our model that present opportunities for more detailed comparisons with experimental data. Drummond and Israelachvili [28] have been able to study transition to stick-slip for a few values of the compliance over a limited range. We hope this initial, exploratory study will be followed by a more complete set of measurements to compare with our predictions.

Recent experimental results by Gourdon and Is-

raelachvili [32] have focused on the temperature and pressure dependence of the transition to stick-slip. While these variables are more accessible experimentally than compliance, they present greater challenges for theory, and cannot be addressed directly here because temperature and pressure do not appear explicitly in the constitutive laws we consider. However, a recent derivation of similar equations [55] provides new theoretical insights for temperature and pressure dependence, suggesting future opportunities to extend our current analysis in this direction.

A quantity which arose in several contexts throughout this paper was the critical strain rate  $\dot{\epsilon}^*$ , beyond which the value of  $\chi$  cannot reach steady state. In our equations, above  $\dot{\epsilon}^*$ ,  $\chi$  diverges with time, because the internal (bounded transition rate) relaxation dynamics cannot keep pace with the rate energy is added to the system. While an actual divergence of  $\chi$  may be impeded by various physical mechanisms (which we did not attempt to incorporate), we believe that the existence of a change of behavior at some high strain rate is physically meaningful, and likely to be an important property that it is closely related to the existence of a latency time in stop-start tests. Because transformation rates are bounded, at high strain rates, the underlying state variable is expected to decouple from the relation between stress and strain rates. This decoupling and has several consequences: (i) since the shear rate is only weakly dependent on state variables, and since it is an increasing function of the stress, velocity strengthening behavior emerges. (ii) The state variable is hidden, its value cannot be deduced from the relation between stress and strain rate, and measurements of apparent steady relationships between stress and strain rate may not correspond to a true steady state. (iii) The hidden value of the state variable depends on the strain. (iv) When the deformation is interrupted, the state variable requires some time before it reaches a sufficiently low value for it to make a measurable impact that can be probed by the emergence of a transient peak (i.e. a stiction spike) in stress. In this case, the latency time becomes a function of the overall strain. If a high strain rate fixed point is reached by the state variable, this dependence disappears, and the latency time should only depend on strain rate. It would therefore be particularly interesting to see whether the underlying dynamics of a state variable can be probed in experiments close to and above  $\dot{\epsilon}^*$  and whether it is consistent with either the emergence of a high strain rate fixed point, or with unstationary dynamics of the state of the lubricated contact. Velocity strengthening has not been observed with the SFA, probably because of intrinsic limits due to the finite scan length. Therefore, it is likely that the high strain rate regimes we discuss here cannot be directly accessed with this experimental setup. However, velocity strengthening has been observed in numerics, [7] and recently in

the experiments [34] by Bureau and coworkers. This latter experimental set-up is constructed to allow sliding over longer distances, and provides access to higher drive velocities than those available with the SFA. It thus may present opportunities to probe some phenomena which arise at high velocities.

Finally, we note that the constitutive equations presented here are derived from heuristic assumptions, which extend STZ theory to the rearrangements occurring inside the sheared material in a lubricated contact. Although our approach is phenomenological, it relies on a specific picture of the microscopic and mesoscopic mechanisms of deformation, and thus forms a bridge between macroscopic, empirical, descriptions and a fundamental understanding of the microscopic physics. The STZ picture of plastic rearrangements occurring in localized zones is supported by numerical observations [56]. However, it would be useful to also image rearrangements in experimental situations. Although the SFA provides a very well-controlled environment at the microscopic level, it seems unlikely that such atomistic imaging of the lubricant could be performed. Other materials are more likely candidates for such observations. Indeed, the picture of elementary rearrangements which emerges here is not limited to lubricants, but is expected to apply to a wide range of amorphous materials, in particular colloidal suspensions and granular materials. Indeed, recent experiments by Gollub have imaged local rearrangements in granular bead packs forming the interfacial material in friction measurements. These experiments also exhibit stick-slip at low drive velocities, and a transition to steady sliding as the drive rate is increased. [49, 50, 51] A further theoretical challenge associated with these measurements arises because slip does not occur homogeneously in the material, but rather is primarily restricted to a relatively narrow dilatant region near the top of the bead pack. We expect the results presented here may extend to other types of amorphous materials, but in situations when strain localization does not preempt the application of a homogeneous description. Colloids and granular materials may provide simultaneous access to macroscopic rheological properties, and microscopic imaging of elementary rearrangements.

This work was supported by the W. M. Keck Foundation, and the NSF Grant No. DMR-9813752, and EPRI/DoD through the Program on Interactive Complex Networks.

## APPENDIX I: HOPF ANALYSIS

We present here the details of the calculation of the Hopf bifurcation. For the stress-linear free-volume constitutive equations (14) and (15). The complete dynam-

ical studied can be rewritten as:

$$\dot{\sigma} = \mu \left( \dot{\epsilon} - E_0 \exp \left[ -\frac{1}{\chi} \right] \sigma \right) \quad (35)$$

$$\dot{\chi} = -E_1 \exp \left[ -\frac{\kappa}{\chi} \right] + \alpha E_0 \exp \left[ -\frac{1}{\chi} \right] \sigma^2 \quad (36)$$

The calculation of the Hopf bifurcation point is straightforward: it amounts to considering the trace of the Jacobian of this dynamical system. However, the calculation identifying the critical Hopf point  $\mu_{crit}$  dividing the sub- and super-critical bifurcation lines requires more lengthy calculations and benefits from the introduction of simplifying notation. Let us write the equations as:

$$\dot{\sigma} = \mu (\dot{\epsilon} - f_1(\chi) \sigma) \quad (37)$$

$$\dot{\chi} = -f_2(\chi) + \alpha f_1(\chi) \sigma^2 \quad (38)$$

and perform the analysis in this more general framework.

The stationary solution is determined by

$$\sigma^2 \equiv S(\chi) = \frac{f_2(\chi)}{\alpha f_1(\chi)} \quad , \quad (39)$$

and

$$\dot{\epsilon}^2 \equiv E(\chi) = \frac{f_1(\chi) f_2(\chi)}{\alpha} \quad (40)$$

where the functions  $E$  and  $S$  have been introduced for future convenience. In the case of equations (35) and (36), these functions are:

$$E(\chi) = \frac{E_0 E_1}{\alpha} \exp \left[ -\frac{\kappa + 1}{\chi} \right] \quad , \quad (41)$$

and

$$S(\chi) = \frac{E_1}{\alpha E_0} \exp \left[ -\frac{\kappa - 1}{\chi} \right] \quad . \quad (42)$$

The Jacobian of this dynamical system reads:

$$J = \begin{pmatrix} -\mu f_1(\chi) & -\mu f_1'(\chi) \sigma \\ 2\sigma f_1(\chi) & -f_2'(\chi) + \sigma^2 f_1'(\chi) \end{pmatrix} \quad , \quad (43)$$

and around the stationary solution, the eigenvalues of the Jacobian satisfy:

$$\lambda^2 + \lambda \sqrt{\frac{E(\chi)}{S(\chi)}} (\mu + \alpha S'(\chi)) + \alpha \mu E'(\chi) = 0 \quad . \quad (44)$$

The Hopf bifurcation occurs when

$$\mu = -\alpha S'(\chi) \quad , \quad (45)$$

at any point where  $E(\chi)$  is strictly increasing. In our case,  $E$  is always an increasing function of  $\chi$ , and  $S$  is a decreasing function of  $\chi$  if and only if  $\kappa < 1$ . If  $S$  is an increasing function of  $\chi$  ( $\kappa > 1$ ) – which also means that

$S \circ E^{-1}$  is an increasing function of  $\dot{\epsilon}$ , there is no Hopf bifurcation, and the steady sliding motion is stable. If  $\kappa < 1$ ,  $S$  is a decreasing function of  $\chi$ ; for any  $\dot{\epsilon}$ , there is a critical value of  $\mu$  where the system undergoes a Hopf bifurcation:

$$\begin{aligned} \mu_{\text{hopf}} &= -\alpha S'(E^{-1}(\dot{\epsilon}^2)) \\ &= \frac{E_1}{E_0} \frac{1 - \kappa}{(\kappa + 1)^2} \left( \frac{\alpha \dot{\epsilon}^2}{E_0 E_1} \right)^{\frac{\kappa-1}{\kappa+1}} \ln \left[ \frac{\alpha \dot{\epsilon}^2}{E_0 E_1} \right]^2 \quad . \end{aligned}$$

In order to determine the type of Hopf bifurcation (super- or sub-critical), we write our non-linear system of ODE's in normal form. For this purpose, we look for the linear operator  $T$  which transforms the Jacobian as:

$$T^{-1} J T = \begin{pmatrix} \rho & -i\omega \\ i\omega & \rho \end{pmatrix} \quad (46)$$

where the eigenvalues of the Jacobian are  $\lambda_{\pm} = \rho \pm i\omega$ . We also have

$$\rho = -\frac{1}{2} \sqrt{\frac{E(\chi)}{S(\chi)}} (\mu + \alpha S'(\chi)) \quad (47)$$

and

$$\omega^2 = -\rho^2 + \alpha \mu E'(\chi) \quad . \quad (48)$$

The complex eigenvectors associated with  $\lambda_{\pm}$  are

$$u_{\pm} = \begin{pmatrix} -\frac{\rho \pm i\omega}{2\alpha \sqrt{E(\chi)}} - \frac{\mu}{2\alpha \sqrt{S(\chi)}} \\ 1 \end{pmatrix} \quad , \quad (49)$$

and  $T$  is obtained from the real and imaginary parts of these complex eigenvectors,  $u_r = \text{Re}(u_+)$ ,  $u_i = \text{Im}(u_+)$

$$\begin{aligned} T &= (u_r \ u_i) \\ &= \begin{pmatrix} -\frac{1}{2\alpha} \left( \frac{\mu}{\sqrt{S(\chi)}} + \frac{\rho}{\sqrt{E(\chi)}} \right) & -\frac{1}{2\alpha} \frac{\omega}{\sqrt{E(\chi)}} \\ 1 & 0 \end{pmatrix} \end{aligned}$$

and

$$T^{-1} = \begin{pmatrix} 0 & 1 \\ -2\alpha \frac{\sqrt{E(\chi)}}{\omega} & -\frac{\rho}{\omega} - \frac{\mu}{\omega} \sqrt{\frac{E(\chi)}{S(\chi)}} \end{pmatrix} \quad . \quad (50)$$

The condition  $\rho = 0$  determines the Hopf bifurcation, and at this point, the transformations  $T$  and  $T^{-1}$  reduce to,

$$T = \begin{pmatrix} \frac{S'(\chi)}{2\sqrt{S(\chi)}} & -\frac{1}{2} \sqrt{-\frac{S'(\chi)E'(\chi)}{E(\chi)}} \\ 1 & 0 \end{pmatrix} \quad (51)$$

and

$$T^{-1} = \begin{pmatrix} 0 & 1 \\ 2\sqrt{-\frac{E(\chi)}{S'(\chi)E'(\chi)}} & -\sqrt{-\frac{S'(\chi)E(\chi)}{S(\chi)E'(\chi)}} \end{pmatrix} \quad (52)$$

Next, we implement the linear change of variables,

$$\begin{pmatrix} x \\ y \end{pmatrix} = T^{-1} \begin{pmatrix} \sigma - \sigma_0 \\ \chi - \chi_0 \end{pmatrix} \quad (53)$$

which leads to the system of ODE's,

$$\begin{pmatrix} \dot{x} \\ \dot{y} \end{pmatrix} = \begin{pmatrix} \rho & -\omega \\ \omega & \rho \end{pmatrix} \begin{pmatrix} x \\ y \end{pmatrix} + \begin{pmatrix} f(x, y) \\ g(x, y) \end{pmatrix} \quad (54)$$

The stability coefficient  $a$  determines whether the bifurcation is super- or sub-critical. In normal form, this coefficient can be directly obtained from the derivatives of the functions  $f$  and  $g$ :

$$\begin{aligned} a &= \frac{1}{16} (f_{xxx} + f_{xyy} + g_{xxy} + g_{yyy}) \\ &+ \frac{1}{16\omega} (f_{xy}(f_{xx} + f_{yy}) \\ &\quad - g_{xy}(g_{xx} + g_{yy}) - f_{xx}g_{xx} + f_{yy}g_{yy}) \end{aligned}$$

We then obtain, at the Hopf bifurcation point,

$$\begin{aligned} f_{xx} &= \frac{\alpha\sqrt{E(\chi)}(S'(\chi)^2 - 2S(\chi)S''(\chi))}{2S(\chi)^{3/2}} \\ f_{xy} &= \frac{\alpha\sqrt{-S'(\chi)}E'(\chi)}{2E(\chi)} \\ f_{yy} &= -\frac{\alpha S'(\chi)E'(\chi)}{2\sqrt{S(\chi)}\sqrt{E(\chi)}} \\ g_{xx} &= \frac{\alpha\sqrt{-S'(\chi)}(E'(\chi)^2 - 2E(\chi)E''(\chi))}{2E(\chi)\sqrt{E'(\chi)}} \\ g_{xy} &= -\frac{\alpha\sqrt{E(\chi)}S'(\chi)^2}{S(\chi)^{3/2}} \\ g_{yy} &= \frac{\alpha S'(\chi)\sqrt{-S'(\chi)}\sqrt{E'(\chi)}}{2S(\chi)} \\ f_{xxx} &= -\frac{3\alpha\sqrt{E(\chi)}S'(\chi)}{4\sqrt{S(\chi)}} \left( \frac{S'(\chi)}{S(\chi)} - \frac{E'(\chi)}{E(\chi)} \right) \\ &\quad \times \left( \frac{S'(\chi)}{S(\chi)} - 2\frac{S''(\chi)}{S(\chi)} \right) \\ &\quad - \frac{\alpha\sqrt{E(\chi)}S^{(3)}(\chi)}{\sqrt{S(\chi)}} \\ f_{xyy} &= \frac{\alpha S'(\chi)E'(\chi)(E(\chi)S'(\chi) - S(\chi)E'(\chi))}{4S(\chi)^{3/2}E(\chi)^{3/2}} \\ g_{yyy} &= 0 \\ g_{xxy} &= \frac{\alpha S'(\chi)^2(E(\chi)S'(\chi) - S(\chi)E'(\chi))}{2S(\chi)^{5/2}\sqrt{E(\chi)}} \end{aligned}$$

whence,

$$\begin{aligned} a &= \frac{\alpha\sqrt{E(\chi)}S''(\chi)}{32S(\chi)^{1/2}} \left( 3\frac{S'(\chi)}{S(\chi)} - 3\frac{E'(\chi)}{E(\chi)} \right. \\ &\quad \left. + 2\frac{E''(\chi)}{E'(\chi)} - 2\frac{S^{(3)}(\chi)}{S''(\chi)} \right) \end{aligned}$$

We thus obtain a quite simple condition for the vanishing of  $a$ , which determines the points where the super- or sub-critical character of the Hopf bifurcation change:

$$\frac{S^{(3)}(\chi)}{S''(\chi)} = \frac{1}{2} \left( \frac{3S'(\chi)}{S(\chi)} - \frac{3E'(\chi)}{E(\chi)} + \frac{2E''(\chi)}{E'(\chi)} \right) \quad (55)$$

With the specific functions  $E$  and  $S$  of our current interest, the parameter  $a$  reads,

$$a = \frac{1}{16\chi^6} \exp \left[ -\frac{\kappa}{\chi} \right] E_1(1 - \kappa) (\kappa - 1 - 2\kappa\chi + 2\chi^2) \quad , \quad (56)$$

which admits a single positive zero for  $\kappa < 1$ :

$$\chi_{\text{crit}} = \frac{1}{2} \left( \kappa + \sqrt{2 - 2\kappa + \kappa^2} \right) \quad (57)$$

This value defines a critical value for the parameter  $\mu$  at the Hopf bifurcation,

$$\begin{aligned} \mu_{\text{crit}} &= \frac{E_1}{E_0} \frac{1 - \kappa}{\chi_{\text{crit}}^2} \exp \left[ \frac{1 - \kappa}{\chi_{\text{crit}}} \right] \\ &= \frac{E_1}{E_0} \frac{e^{-\kappa + \sqrt{2 - 2\kappa + \kappa^2}}}{1 - \kappa} \left( \kappa - \sqrt{2 - 2\kappa + \kappa^2} \right)^2 \end{aligned}$$

and the critical strain rate,

$$\dot{\epsilon}_{\text{crit}} = \sqrt{\frac{E_1 E_0}{\alpha}} \exp \left[ -\frac{\kappa + 1}{\kappa - 1} \left( \kappa - \sqrt{2 - 2\kappa + \kappa^2} \right) \right]$$

- 
- [1] R. G. Horn and J. N. Israelachvili, *J. Chem. Phys.* **75**, 1400 (1981).
  - [2] H. K. Christenson, D. W. R. Gruen, R. G. Horn, and J. N. Israelachvili, *J. Chem. Phys.* **1834**, 1400 (1987).
  - [3] J. Israelachvili, P. McGuiggan, and A. Homola, *Science* **240**, 189 (1988).
  - [4] M. Schoen, C. L. Rhykerd, D. J. Diesler, and J. H. Cushman, *Science* **245**, 1223 (1989).
  - [5] M. L. Gee, P. M. McGuiggan, J. N. Israelachvili, and A. M. Homola, *J. Chem. Phys.* **93**, 1895 (1990).
  - [6] P. A. Thompson and M. O. Robbins, *Phys. Rev. A* **41**, 6830 (1990).
  - [7] P. A. Thompson and M. O. Robbins, *Science* **250**, 792 (1990).
  - [8] S. Grannick, *Science* **253**, 1374 (1991).
  - [9] M. W. Ribarsky and U. Landman, *J. Chem. Phys.* **97**, 1937 (1992).
  - [10] P. A. Thompson, G. S. Grest, and M. O. Robbins, *Phys. Rev. Lett.* **68**, 3448 (1992).
  - [11] I. A. Bitsanis and C. Pan, *J. Chem. Phys.* **99**, 5520 (1993).
  - [12] B. N. Persson, *Phys. Rev. Lett.* **71**, 1212 (1993).
  - [13] M. J. Stevens and M. O. Robbins, *Phys. Rev. E* **48**, 3778 (1993).
  - [14] H. Yoshizawa, P. McGuiggan, and J. Israelachvili, *Science* **259**, 1305 (1993).
  - [15] H. Yoshizawa and J. Israelachvili, *J. Phys. Chem.* **97**, 11300 (1993).

- [16] G. Reiter *et al.*, J. Chem. Phys. **101**, 2606 (1994).
- [17] B. N. Persson, Phys. Rev. B **50**, 4771 (1994).
- [18] Y. B. Mel'nichenko, J. Schüller, R. Richert, and B. Ewen, J. Chem. Phys. **103**, 2016 (1995).
- [19] M. Urbakh, L. Daikhin, and J. Klafter, Phys. Rev. E **51**, 2137 (1995).
- [20] J. M. Carlson and A. A. Batista, Phys. Rev. E **53**, 4153 (1996).
- [21] J. Gao, W. Luedtke, and U. Landman, J. Chem. Phys. **106**, 4309 (1996).
- [22] A. L. Demirel and S. Granick, Phys. Rev. Lett. **77**, 2261 (1996).
- [23] J. Gao, W. Luedtke, and U. Landman, Phys. Rev. Lett. **79**, 705 (1997).
- [24] G. Luengo, F.-J. Schmitt, R. Hill, and Jacob Israelachvili, Macromolecules **30**, 2482 (1997).
- [25] M. G. Rozman, M. Urbakh, J. Klafter, and F.-J. Elmer, J. Phys. Chem. B **102**, 7924 (1998).
- [26] A. A. Batista and J. M. Carlson, Phys. Rev. E **57**, 4986 (1998).
- [27] Persson, in *Sliding Friction : Physical Principles and Applications (Nanoscience and Technology)*, edited by "" (Springer Verlag, "", 2000).
- [28] C. Drummond and J. Israelachvili, Macromolecules **33**, 4910 (2000).
- [29] L. Berthier and J.-L. Barrat, Phys. Rev. E **63**, 012503 (2001).
- [30] C. Drummond and J. Israelachvili, Phys. Rev. E **63**, 041506 (2001).
- [31] L. Berthier and J.-L. Barrat, Phys. Rev. Lett. **89**, 095702 (2002).
- [32] D. Gourdon and J. Israelachvili, Phys. Rev. E **68**, 021602 (2003).
- [33] M. Robbins, Shear yielding of amorphous glassy solids: Effect of temperature and strain rate, cond-mat/0303276, 2003.
- [34] L. Bureau, T. Baumberger, and C. Caroli, Rheological aging and rejuvenation in solid friction contacts, cond-mat/0202245, 2002.
- [35] A. Lemaitre, Phys. Rev. Lett. **89**, 195503 (2002).
- [36] A. Lemaitre, A Dynamical Approach to Glassy Materials, cond-mat/0206417, 2002.
- [37] J. Gao, W. Luedtke, and U. Landman, Trib. Lett. **9**, 3 (2000).
- [38] B. N. Persson, Phys. Rev. B **48**, 18140 (1993).
- [39] J. H. Dieterich, Pure Appl. Geophys. **116**, 790 (1978).
- [40] J. H. Dieterich, J. Geophys. Res. **84**, 2161 (1979).
- [41] A. Ruina, J. Geophys. Res. **88**, 10359 (1983).
- [42] J. H. Dieterich and B. D. Kilgore, Pageoph. **143**, 283 (1994).
- [43] J. Rice and A. Ruina, J. Appl. Mech. **105**, 343 (1983).
- [44] J. R. Rice and S. T. Tse, J. Geophys. Res. **91**, 521 (1986).
- [45] T. Baumberger, F. Heslot, and B. Perrin, Nature **367**, 544 (1994).
- [46] F. Heslot *et al.*, Phys. Rev. E **49**, 4973 (1994).
- [47] T. Baumberger, C. Caroli, B. Perrin, and O. Ronsin, Phys. Rev. E **51**, 4005 (1995).
- [48] L. C. E. Struik, *Physical Aging in Amorphous Polymers and Other Materials* (Elsevier, Houston, 1976).
- [49] S. Nasuno, A. Kudrolli, and J. Gollub, Phys. Rev. Lett. **79**, 949 (1997).
- [50] S. Nasuno, A. Kudrolli, A. Bak, and J. Gollub, Phys. Rev. E **58**, 2161 (1998).
- [51] J.-C. Géminard, W. Losert, and J. Gollub, Phys. Rev. E **59**, 5881 (1999).
- [52] W. Losert, J.-C. Géminard, S. Nasuno, and J. Gollub, Phys. Rev. E **61**, 4060 (2000).
- [53] D. Gourdon, private communication.
- [54] A. L. Demirel and S. Granick, Phys. Rev. Lett. **77**, 4330 (1996).
- [55] A. Lemaitre, "Out-of-equilibrium relaxation of a time-dependent effective temperature", cond-mat/0307216, 2002.
- [56] M. L. Falk and J. S. Langer, Phys. Rev. E **57**, 7192 (1998).
- [57] M. L. Falk and J. S. Langer, M.R.S. Bulletin **25**, 40 (2000).
- [58] M. L. Falk, Phys. Rev. B **60**, 7062 (1999).
- [59] F. Spaepen, Acta Metall. **25**, 407 (1977).
- [60] A. Argon, Acta Metall. **27**, 47 (1979).
- [61] A. Argon and H. Kuo, Mater. Sc. Eng. **39**, 101 (1979).
- [62] F. Spaepen and A. Taub, in *Les Houches Lectures XXXV on Physics of Defects, Les Houches Lectures, Session XXXV*, edited by J.-P. Balian and M. Kleman (North-Holland, Amsterdam, 1981), p. 133.
- [63] A. Argon and L. Shi, Acta Metall. **31**, 499 (1983).
- [64] A. K. Doolittle, J. Appl. Phys. **22**, 1471 (1951).
- [65] A. K. Doolittle and D. B. Doolittle, J. Appl. Phys. **28**, 901 (1957).
- [66] D. Turnbull and M. H. Cohen, J. Chem. Phys. **34**, 120 (1961).
- [67] D. Turnbull and M. H. Cohen, J. Chem. Phys. **52**, 3038 (1970).
- [68] G. S. Grest and M. H. Cohen, Adv. Chem. Phys. **48**, 455 (1981).
- [69] E. R. Nowak *et al.*, Phys. Rev. E **57**, 1971 (1998).
- [70] T. Boutreux and P. G. de Gennes, Physica A **244**, 59 (1997).
- [71] R. Stinchcombe and M. Depken, Phys. Rev. Lett. **88**, 125701 (2002).
- [72] P. A. Thompson and G. S. Grest, Phys. Rev. Lett. **67**, 1751 (1991).
- [73] T. Becker, in *Geocomplexity and the Physics of Earthquakes*, Vol. 120 of *Geophysical Monograph*, edited by J. Rundle, D. Turcotte, and W. Klein (AGU, ADDRESS, 2000).
- [74] A. Mehta and S. F. Edwards, Physica A **157**, 1091 (1989).
- [75] S. F. Edwards and R. B. S. Oakeshott, Physica A **157**, 1080 (1989).
- [76] S. Edwards, in *Granular Matter: An Interdisciplinary Approach*, edited by A. Mehta (Springer-Verlag, New-York, 1994), pp. 121–140.
- [77] L. F. Cugliandolo and J. Kurchan, **126**, 407 (1997).
- [78] L. F. Cugliandolo, J. Kurchan, and L. Peliti, Phys. Rev. E **55**, 3898 (1997).
- [79] I. K. Ono *et al.*, Phys. Rev. Lett. **89**, 095703 (2002).
- [80] H. A. Makse and J. Kurchan, Nature **415**, 614 (2002).
- [81] K. Maeda and S. Takeuchi, Phys. Stat. Sol. A **49**, 685 (1978).
- [82] K. Maeda and S. Takeuchi, Phil. Mag. A **44**, 643 (1981).
- [83] S. Takeuchi and K. Maeda, Key Eng. Mater. **13-15**, 749 (1987).
- [84] H. Eyring, J. Chem. Phys. **4**, 283 (1936).
- [85] V. Arnold, *Mathematical Methods of Classical Mechanics (Graduate Texts in Mathematics Vol. 60)* (Springer-Verlag, Berlin, Heidelberg, 1974).